Geometrical and Taylor dispersion in a fracture with random obstacles: An experimental study with fluids of different rheologies

A. Boschan,[1,2] I. Ippolito,[1] R. Chertcoff,[1] H. Auradou,[2] L. Talon,[2] and J. P. Hulin[2]

Received 3 August 2007; revised 6 February 2008; accepted 21 February 2008; published 26 June 2008.

[1] The miscible displacement of a Newtonian or shear-thinning fluid by another one of same rheological properties has been studied optically in a flat transparent model fracture with a random distribution of identical cylindrical obstacles on one of the walls. At the local scale, the concentration variation on individual pixels satisfies a Gaussian convection-dispersion relation with local transit time $\bar{t}(x, y)$ and dispersivity $l_d(x, y)$. The variation of l_d with the Péclet number Pe shows that it results from a combination of geometrical and Taylor dispersion, respectively dominant at low and high Pe values. Using shear-thinning solutions instead of a Newtonian fluid enhances the velocity contrasts (and therefore geometrical dispersion) and reduces Taylor dispersion. At the global scale, the front geometry is studied from the isoconcentration lines $c = 0.5$ (equivalent to lines of constant $\bar{t}(x, y)$ value): beyond a transition travel time, their width in the direction parallel to the flow reaches a constant limit varying linearly with $Log(Pe)$ with a slope increasing with the shear-thinning character of the fluid. These characteristics are compared to previous observations on other model fractures with a self-affine roughness displaying channelization effects.

Citation: Boschan, R., I. Ippolito, R. Chertcoff, H. Auradou, L. Talon, and J. P. Hulin (2008), Geometrical and Taylor dispersion in a fracture with random obstacles: An experimental study with fluids of different rheologies, *Water Resour. Res.*, *44*, W06420, doi:10.1029/2007WR006403.

1. Introduction

[2] The transport of dissolved species in fractured formations is an important issue in waste storage or water management applications [*NAS Committee on Fracture Characterization and Fluid Flow*, 1996; *Neretnieks*, 2002]. Obtaining reliable predictions of these processes requires modeling the advection and the dispersion of contaminants from a source inside or at the surface of the fractured rocks [*Adler and Thovert*, 1999; *Berkowitz*, 2002]. Ultimately, these phenomena must be modeled at the scale of the fracture network but understanding transport in a single fracture is a crucial first step.

[3] Fractures have often been represented as the fluid saturated space between two parallel plane surfaces [*Witherspoon et al.*, 1980]. This neglects the strong influence of the variations of the aperture due to the roughness of the walls, resulting in spatial heterogeneities of the mean flow in the plane of the fracture [*Tsang and Tsang*, 1987; *Brown et al.*, 1998]. This roughness may display very different geometrical features depending on the origin of the fracture and of its subsequent history (flow, physicochemical processes, etc.).

[4] A first case is surfaces with multiple characteristic length scales observed in many fractured rocks [*Bouchaud*, 2003]. Several studies dealt for instance with fractures bound by complementary self-affine surfaces with a relative shear displacement [*Gentier et al.*, 1997; *Yeo et al.*, 1998; *Auradou et al.*, 2005]. In this case, the fracture aperture field is structured into long preferential channels perpendicular to the shear. Experimental studies of miscible fluid displacements using dyed fluids have been reported in transparent models with this geometry [*Auradou et al.*, 2006; *Boschan et al.*, 2007]. The large scale structure of the displacement front reflects the velocity contrasts between the preferential channels and its width parallel to the flow increases linearly with time. Global front spreading is then dominantly convective and controlled by the large scale structures of the velocity field rather than by its local disorder.

[5] The present experimental work uses a similar technique but applied to rough fractures of different geometry featuring a short correlation length of the velocity fluctuations and no large scale channels: these models have two plane walls with a random distribution of cylindrical obstacles of uniform size over one of them. This geometry allowed us to study the interplay of the mechanical and Taylor dispersion mechanisms which are both present in these models and depend differently on the flow velocity.

[6] The second focus of this work is on the influence of the fluid rheology. The two dispersion mechanisms [*Paterson et al.*, 1996; *Auradou et al.*, 2006] are altered in opposite directions when Newtonian fluids are replaced by shear thinning solutions: while mean velocity contrasts

[1]Grupo de Medios Porosos, Facultad de Ingeniería, Universidad de Buenos Aires, Buenos Aires, Argentina.

[2]Laboratoire Fluides, Automatique et Systèmes Thermiques, CNRS, Université Pierre et Marie Curie-Paris 6, Université Paris Sud, Orsay Cedex, France.

0043-1397/08/2007WR006403$09.00

between different flow paths (and therefore geometrical dispersion) is enhanced for shear-thinning fluids, the velocity profiles in individual flow channels flatten out, reducing therefore Taylor dispersion [*Vartuli et al.*, 1995]. The results obtained in the present work may be relevant to different water management problems such as the spreading of complex pollutants or decontamination processes using fluids such as concentrated colloidal dispersions, emulsions or foams [see, e.g., *Bragato and El Seoud*, 2003; *Borden*, 2007]. These may indeed display non-Newtonian rheological characteristics influencing strongly their propagation through porous and/or fractured media.

[7] In the following, the main dispersion mechanisms and the experimental setup and procedure are first described: using a dyed and a transparent fluid for the displacements allows for optical measurements of their local relative concentration and of its variation with time at a scale smaller than the roughness size. Using these measurements, the dispersion of the dye tracer is studied at the local and global scales as a function of the Péclet number *Pe* and for different Newtonian and polymer solutions. The relative influence of the different dispersion mechanisms is then analyzed and additional information is obtained from an analysis of the local structure of the displacement front.

2. Dispersion Mechanisms in Fractures

[8] In homogeneous porous media inside which a flow of mean velocity U has been established, the concentration $c(x,t)$ of a tracer (assumed to be constant in the directions perpendicular to the orientation x of the velocity) often satisfies the Fickian advection-dispersion equation:

$$\frac{\partial c}{\partial t} + U\frac{\partial c}{\partial x} = D\frac{\partial^2 c}{\partial x^2}. \tag{1}$$

where D is the longitudinal dispersion coefficient which is often replaced by the dispersivity $l_d = D/U$. The same equation may be expected to be valid in fractures, particularly when no preferential channels are present (c is then an average of the local concentration across the fracture gap). Several numerical, theoretical and experimental investigations suggest that the variation of the normalized dispersivity with the Péclet number *Pe* should be of the form [*Ippolito et al.*, 1993, 1994; *Roux et al.*, 1998; *Adler and Thovert*, 1999; *Detwiler et al.*, 2000]:

$$\frac{l_d}{a} = \alpha_G + \alpha_T Pe. \tag{2}$$

In this expression, $Pe = Ua/D_m$ in which a is the mean fracture aperture and D_m is the molecular diffusion. In this equation, *Pe* is assumed to be larger than 1 so that pure longitudinal molecular diffusion is negligible (a $1/Pe$ term would otherwise have to be added).

[9] The $\alpha_T Pe$ term corresponds to Taylor dispersion: it results from the spreading of the tracer (for instance dye) by the velocity profile between the plates balanced by transverse molecular diffusion across the gap [*Taylor*, 1953; *Aris*, 1956]. For a fracture with two flat parallel walls and for Newtonian fluids, $\alpha_G = 0$ and $\alpha_T = 1/210$; the value of α_T should be lower for shear-thinning fluids due to the flattening of the velocity profile between the walls [*Vartuli et al.*, 1995; *Boschan et al.*, 2003].

[10] The α_G term is nonzero only for fracture with rough walls and reflects the influence of geometrical dispersion. It is due to spatial variations of the flow velocity in the plane of the fracture. Its value has been predicted [*Gelhar*, 1993; *Roux et al.*, 1998] to scale as:

$$\alpha_G = B\frac{\xi\epsilon^2}{a}. \tag{3}$$

in which $\varepsilon = \sigma_u/U$ characterizes the amplitude of the fluid velocity fluctuations and ξ their correlation length in the flow direction (σ_u is the standard deviation of the fluid velocity from its mean value U). In the previous equation, the value of the constant B depends on the aperture distribution; for a Gaussian aperture field, it is equal to $2/\sqrt{\pi}$. Such a diffusive spreading regime can only be reached when the correlation length of the velocity field is small enough compared to the size of the sample. This condition will be satisfied for the models used in the present work; this was not the case for the self-affine fractures used by *Boschan et al.* [2007] in which preferential channels with a length of the order of that of the fracture were present. From equation (2), the relative influence of Taylor dispersion may be expected to be larger at high Péclet numbers with geometrical dispersion being dominant at low flow velocities (although still with $Pe > 1$). Also, and in contrast with Taylor dispersion, α_G may be expected to be larger for shear-thinning fluids due to the enhancement of the spatial velocity variations inside the model fracture. A similar increase, is observed in the self affine fractures [*Boschan et al.*, 2007], this time for the velocity contrasts between slow and preferential channels.

3. Experimental Setup and Procedure

3.1 Model Fracture and Displacement Experiments

[11] The model fracture corresponds to the space between two transparent surfaces. The upper one is a flat glass plate and the lower one is a rough photopolymer plate lying against a flat glass backing (see Figure 1). The wall roughness is represented by randomly distributed cylindrical obstacles protruding out of the plane surface. Their layout has been generated by computer: there are 5400 obstacles of diameter d_o = 1.4 mm and height 0.35 mm, covering 20% of the wall area. The minimum distance between the centers of the obstacles is 2.1 mm (1.5 times the diameter of the obstacle) and its mean is 3.6 mm. The layout is first printed onto the photopolymer plate using an *UV* light source and the obstacles are then revealed by etching. Their height may be adjusted by varying the duration of the exposure to the *UV* light.

[12] The two fracture walls are kept apart by mylar spacers with a size: 350 mm × 20 mm. These are located on the two longer parallel sides of the model and also act as seals. The size of the remaining useful area of the fracture is: 350 × 120 mm. The mean aperture a of the fracture is defined as the ratio of the volume accessible to the fluid in the fracture and of the corresponding area of the wall. This fluid volume is measured independently by filling it using a calibrated syringe pump, leading to $a = 0.65 \pm 0.02$ mm. Another estimation of a is also obtained from the velocity of the displacement fronts during the experiments: these fronts

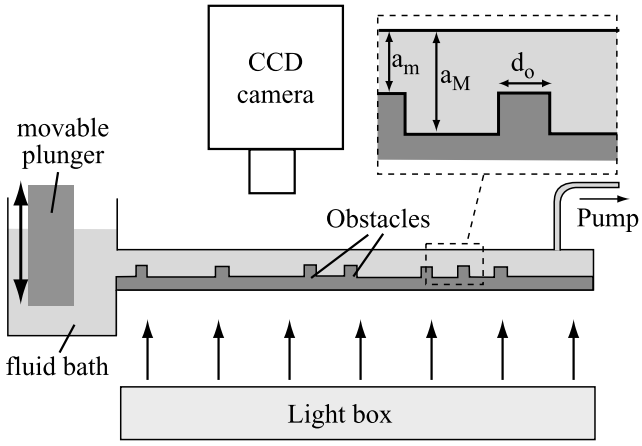

Figure 1. Schematic view of the experimental setup and fracture model.

are straight and parallel to the y direction, implying that there is no sizable gradient of the mean aperture across the width of the model. The value of a is used to define the Péclet number with:

$$Pe = \frac{Ua}{D_m} \tag{4}$$

in which U is the average velocity in the gap (equal to the mean velocity of the front).

[13] The minimum aperture a_m of the model (i.e., the distance between the top of the obstacles and the flat glass plate) and its maximum a_M are determined by measuring the height of the obstacles and the thickness of the spacers with a mechanical caliper. The corresponding values are respectively: $a_m = 0.37 \pm 0.02$ mm and $a_M = 0.72 \pm 0.02$ mm. The lack of mechanical contact points in the model (i.e., the fact that $a_m > 0$) allows for simpler interpretations due to the narrower distribution of the transit times through the different regions of the fracture. An independent value of a is provided by the weighted average of a_m and a_M using the fraction of the area corresponding to each of these two apertures; this value of a agrees within ±5% with the two previous ones.

[14] The fracture assembly is horizontal with the two longer sides sealed by the spacers while the shorter ones are open to allow for fluid flow in and out of the fracture. The inlet side is attached to a fluid reservoir with an open surface; the outlet is connected to a syringe pump sucking the solutions out of the fracture at a selectable constant flow rate. The procedure for saturating the model and obtaining a straight sharp initial displacement front is very similar to that described in a previous paper for vertical models [*Boschan et al.*, 2007]. By repeating this procedure, sequences of "direct" experiments in which the dyed fluid displaces the clear one and "inverse" experiments in which the dyed fluid is displaced are realized. In order to avoid pollution by outside dust, the aperture of the reservoir is kept covered during the experiments.

[15] For each solution selected, both direct and inverse displacement experiments have been realized at 7 different constant flow rates ranging between 0.014 and 1.4 ml/min ($3 < Pe < 350$). Depending on the flow rate, the duration of the experiments required to obtain a complete saturation of the fracture by the invading fluid ranges between 24 min and 42 h.

3.2. Fluid Preparation and Characterization

[16] The solutions used in the present work are either a Newtonian water-glycerol mixture or shear-thinning water-polymer (scleroglucan) solutions with a 500 or 1000 ppm polymer concentration. In all cases, the injected and displaced fluids have identical rheological properties. The Newtonian solution contains 10% in weight of glycerol and has a viscosity equal to 1.3×10^{-3} Pa·s at 20°.

[17] The preparation and characteristics of the shear-thinning solutions are the same as reported by *Boschan et al.* [2007]. The variation of the viscosity η with the shear rate $\dot{\gamma}$ is well fitted by the Carreau function:

$$\eta = \frac{1}{\left(1 + \left(\frac{\dot{\gamma}}{\dot{\gamma}_0}\right)^2\right)^{\frac{1-n}{2}}}(\eta_0 - \eta_\infty) + \eta_\infty. \tag{5}$$

[18] The values of the parameters of this equation for the two solutions used here are listed in Table 1. At low shear rates $\dot{\gamma} \lesssim \dot{\gamma}_0$, the viscosity is constant like for a Newtonian fluid with $\eta \simeq \eta_0$ (Newtonian plateau regime). At higher shear rates $\dot{\gamma} \gtrsim \dot{\gamma}_0$, the variation of the viscosity follows a power law: $\eta \propto \dot{\gamma}^{(n-1)}$. The viscosity η should reach a limiting value η_∞ at still higher shear rates, much beyond the experimental range; practically η_∞ is taken equal to 1 mPa·s, i.e., the viscosity of water (the solvent).

[19] For flow between parallel plates separated by a distance a, the velocity profile in the gap can be computed easily from the relation between $\dot{\gamma}$ and η [*Bird et al.*, 1987]. Compared to the well known parabolic shape for Newtonian fluids, the velocity profile for a shear-thinning solution is flatter in the low shear rate region located halfway between the plates. The shear rate has its maximum value $\dot{\gamma}_w$ at the walls. At low flow velocities, one has $\dot{\gamma}_w \leq \dot{\gamma}_0$ and the flow profile is the same as for a Newtonian fluid with $\dot{\gamma}_w = 6U/a$. At higher velocities for which $\dot{\gamma}_w \geq \dot{\gamma}_0$ the shear thinning characteristics become important and, for a given mean velocity U, one has $\dot{\gamma}_w > 6U/a$ [*Gabbanelli et al.*, 2005]. Using the above expression of $\dot{\gamma}_w$, the values of the Péclet numbers Pe^* for which $\dot{\gamma}_w \simeq \dot{\gamma}_0$ the regions between the obstacles have been estimated and are respectively of the order of 10 and 30 for the 1000 ppm and 500 ppm solutions.

3.3. Optical Relative Concentration Measurements

[20] The technique used for mapping the relative concentration of the two fluids has been described in a previous paper [*Boschan et al.*, 2007]. The transparent fracture is back illuminated by a light panel (Figure 1): about 100 images of the distribution of the light intensity $I(x, y, t)$ transmitted through the fracture are recorded at constant intervals during the fluid displacement using a *Roper*

Table 1. Rheological Parameters and Characteristic Péclet Numbers for Scleroglucan Solutions Used in the Flow Experiments

C_{poly} ppm	n	$\dot{\gamma}_0$ s^{-1}	η_0 *mPa.s*
500	0.38 ± 0.04	0.077 ± 0.018	410 ± 33
1000	0.26 ± 0.02	0.026 ± 0.004	4500 ± 340

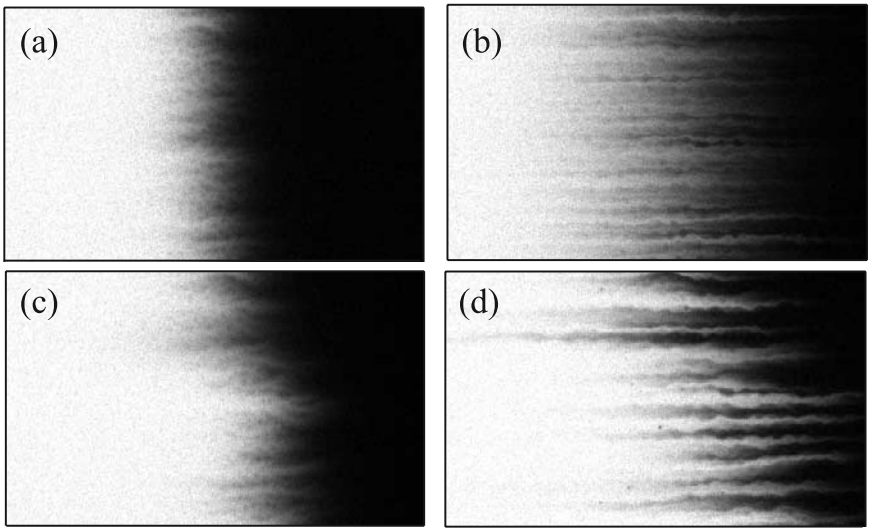

Figure 2. Concentration maps (gray levels code) of a dyed fluid (light shade) displacing a clear one (dark shade). (a–b) Water-glycerol mixture ((a) Pe = 8.6, (b) Pe = 450). (c–d) 1000 ppm polymer solution. ((c) Pe = 6.6, (d) Pe = 345). Mean flow is horizontal on the figure and from left to right. The field of view is 130 mm × 60 mm. The picture is centered in the width of the model and its left side is at a distance of 120 mm from the inlet.

Coolsnap cf digital camera with a high, 12 bits, dynamic range. Reference images with the fracture saturated with the clear and dyed fluids (dye concentration c_0) are also recorded before the experiments and after the full saturation by the displacing fluid. A calibration curve is obtained independently through separate measurements using, in the same fracture, different solutions with dye concentrations ranging from 0.1 to 0.4 g/l. Maps of the local relative dye concentration $0 \leq c(x, y, t)/c_0 \leq 1$ are then obtained after normalizing the experimental images by the reference ones and using the calibration curve (in the following, c_0 is omitted and $c(x,y,t)$ refers directly to the normalized concentration dye concentration). The error on the determination of c is not constant, due to the nonlinear relation between the transmitted light intensity and the dye concentration [see *Boschan et al.*, 2007]: the absolute uncertainty increases from ±1.5% for c = 0.5 to ±5% for c = 1.

4. Qualitative Observations

[21] Figure 2 compares relative concentration maps observed at two different flow rates for both the water glycerol mixture and the 1000 ppm polymer solution (although the flow rates are the same for the two fluids, the Péclet numbers are different because of the difference between the molecular diffusion coefficient). In all cases, the injected volume of the displacing fluid is about half the total fracture volume. In the center part of all four pictures, the variation of the grey shades marks the mixing region where the relative concentration of the colored fluid varies from *0* to *1*. Its variation is not smooth and uniform and small scale filament-like structures approximately parallel to the mean flow are visible. These structures reflect velocity fluctuations between different flow lines: These fluctuations create concentration gradients in the direction transverse to the flow which, in turn, are smoothed out by molecular diffusion. The distance parallel to the flow over which these filaments remain visible is thus largest at high flow rates for which the transit time during which transverse diffusion takes place is reduced while the transverse width of the filaments remains the same. This explains why these filaments are hardly visible for Pe = 6.6 while their length represents a large fraction of that of the model for Pe = 345.

[22] A second important feature is demonstrated by comparing the front structure observed with the water-glycerol and water-polymer solutions. The former displays fine filaments and the front is globally flat. For the shear-thinning fluid, the filaments are coarser and longer and the front displays large scale distortions representing a large fraction of its total width. These distortions are visible at both Péclet numbers while the features of the filaments are mostly visible for Pe = 345.

[23] In the following parts of the paper, two key features of the structure of the mixing zone are analyzed quantitatively for different flow velocities and rheological properties of the fluids.

[24] • In section 5, the local spreading parallel to the mean flow of the concentration variation front (measured on single pixels) is first shown to be well described in all cases by the classical convection-dispersion equation (1). The variations of the corresponding local dispersivity $l_d = D/U$ with Pe are then compared to the predictions of equation (2) and the relative contributions of the geometrical and Taylor mechanisms are discussed.

[25] • In section 6, the structure of the mixing zones and its dependence on the transverse variations of the velocity are characterized from a statistical analysis of the isoconcentration front c = 0.5.

5. Local Spreading of the Mixing Zone

5.1. Quantitative Analysis of Local Concentration Variations

[26] As noted above, the present experimental technique measures variations both with time and distance of the average $c(x,y,t)$ of the local normalized dye concentration

over the aperture. A typical variation of c with time measured experimentally at a fixed point (x, y) is displayed in Figure 3: it is well fitted by the following solution of the convection-dispersion equation (1):

$$c(x,y,t) = \frac{1}{2}\left[1 + erf\,\frac{t-\bar{t}(x,y)}{\sqrt{4\frac{D(x,y)}{U^2}t}}\right]. \quad (6)$$

In the reverse case (clear fluid displacing a dyed solution), the (+) sign should be replaced by a (−) in front of the error function. In equation (6), U is the mean velocity in the whole model, $\bar{t}(x, y)$ the mean transit time and $D(x, y)$ is an effective coefficient reflecting the cumulated dispersion along the trajectories leading from the inlet side of the model to point (x, y). Both $\bar{t}(x, y)$ and $D(x, y)$ depend on the measurement point (x, y). This good fit of the local concentration variation with solutions of the convection-diffusion equation (1) is due to the moderate amplitude of the velocity fluctuations in the model which, itself, results from the relatively narrow distribution of the local apertures. For a model with, for instance, contact points between the wall surfaces (as is often the case in natural fractures), the width of the velocity distribution will increase (due to low velocity regions near the contact points) and the local concentration variation will often not satisfy any more equation (1).

[27] First, for each experiment, the variation with time of the local relative concentration $c(x, y, t)$ of the dyed fluid has been analyzed for each pixel of the image and the corresponding values of $\bar{t}(x, y)$ and $D(x, y)$ have been determined. As will be shown below in section 6, the isoconcentration front $c = 0.5$ at a given time t may be determined from the spatial variations of $\bar{t}(x, y)$ in order to analyze the heterogeneities of the tracer distribution in the mixing zone. The variations of $D(x, y)$ characterize those of the dispersion both across the model and with the distance x from the injection line. The variations with x of the average $\langle D(x, y)\rangle_y$ of $D(x, y)$ across the width of the model are displayed in Figure 4: $\langle D(x, y)\rangle_y$ becomes independent of x after a transition distance of the order of 60 mm for the water-polymer solution while it is shorter than 25 mm for the Newtonian water-glycerol solution. The symmetry of the dispersion process and the influence of buoyancy forces due to residual density contrasts have been checked by realizing the same experiments with the transparent solution displacing the dyed one: this allowed us to invert the buoyancy forces for a same distribution of the injected and displaced fluids. We verified that the values of D for a same distance x remain the same in both configurations.

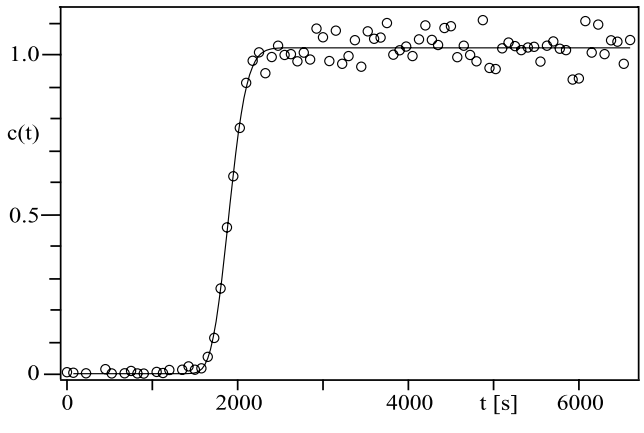

Figure 3. Time variation of the normalized dye concentration $c(x, y, t)$ on a single pixel (x, y) located in the center part of the fracture width at a distance $x = 110$ mm from the inlet (dyed 500 ppm polymer solution displacing the same, clear, solution at $Pe = 69$). Solid line: fit of the data by equation (6) with parameters: $\bar{t}(x, y) = 1902$ s and $D/U^2 = 6.91$ s. The higher noise level at long times when $c(t)$ is close to *1* reflects the larger absolute uncertainty on the concentration discussed at the end of section 3.3.

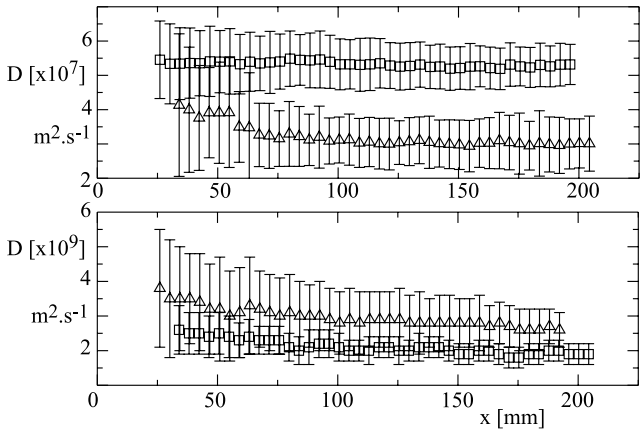

Figure 4. Variation of the average $\langle D(x, y)\rangle_y$ of the local dispersion coefficient as a function of the distance x from the injection line. Water-glycerol mixture (open square): top graph, $Pe = 450$; bottom graph, $Pe = 8.6$. 1000 ppm polymer solution (open triangle): top graph, $Pe = 345$; bottom graph: $Pe = 6.6$. Error bars: standard deviation of the distribution of the *local* values of $D(x, y)$ over the width.

[28] The constant asymptotic value of $\langle D(x, y)\rangle_y$, together with the good fit displayed in Figure 3, suggests that the Fickian dispersion model corresponding to equation (1) describes well the *local spreading* of the front at all locations throughout the experiment. This Fickian spreading process is therefore characterized in the following by the average $D = \langle D(x, y)\rangle_{x,y}$ of the local dispersion coefficient $D(x, y)$.

[29] A similar type of analysis has also been carried out on the average $\langle c(x, y, t)\rangle_y$ of the concentration over the width of the model. The variation of $\langle c(x, y, t)\rangle_y$ with time can also be well fitted by equation (6) which provides a "global" dispersion coefficient D_g. The variation of the ratio D_g/D with the Péclet number Pe is displayed in the inset of Figure 5: for the Newtonian water-glycerol solution and the 500 ppm polymer solution, the ratio can be considered as equal to 1 within experimental error. For the 1000 ppm solution, the ratio is significantly larger than 1 at the highest Péclet numbers: this may indicate an increasing effect of the inhomogeneities of the flow field which are amplified for strongly shear thinning fluids like the 1000 ppm solution (as will be explained in the following sections). It is however difficult to identify the different factors determining the value of D_g. For this reason, in the

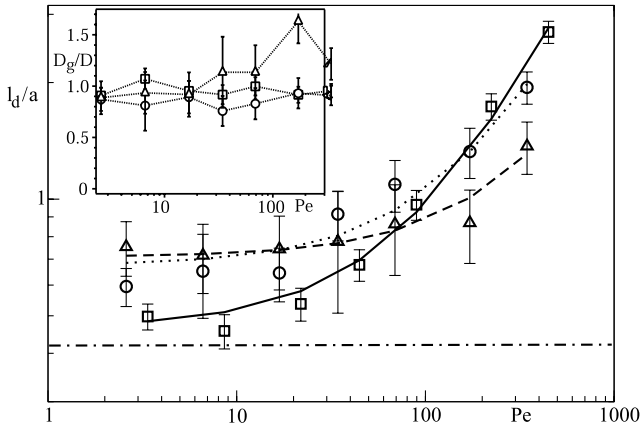

Figure 5. Variation of the experimental dispersivity l_d as a function of the Péclet number (□), water-glycerol solution; (△), 1000 ppm; (○), 500 ppm polymer solutions. Solid, dotted and dashed lines: fit of the respective data with equation (2). Horizontal dash-dotted line: value of α_G estimated by numerical simulation for the Newtonian solution. Inset: variation of the ratio D_g/D of the global and local dispersion coefficients as a function of the Péclet number. The symbols are the same as in the main graph.

following, we analyze separately the "local" dispersion mechanisms and the large scale effects respectively from the variations of the "local" coefficient D and from the front geometry.

[30] In order to identify easily the relative influence of the different dispersion mechanisms, it is more convenient to replace the coefficient D by the dispersivity $l_d = D/U$ (U is the mean flow velocity). In the next section, the variation of l_d is studied as a function of the different flow parameters for the three different Newtonian and shear-thinning solutions investigated in the present work.

5.2. Dispersivity Dependence on the Fluid Velocity and Rheology

[31] The variation of the normalized dispersivity l_d/a is displayed in Figure 5 as a function of the Péclet number $Pe = aU/D_m$ ($a \simeq 0.65$ mm is the mean fracture aperture). For all three solutions, l_d remains initially constant at low Pe values and increases strongly at higher ones (and particularly for $Pe \gtrsim 100$). These experimental variations may be well fitted by equation (2) (lines in Figure 5) and the values of the parameters α_G and α_T corresponding to these fits are listed in Table 2. The variation of l_d with Pe is in agreement with the discussion in section 2 assuming that l_d results from the combination of geometrical and Taylor dispersions: the former is dominant at low Pe values and the latter at higher ones.

[32] From section 2, α_G and α_T should respectively increase and decrease with the shear thinning character of the fluid. At low Péclet numbers, l_d/a is indeed significantly lower for the water-glycerol solution than for the two polymer-water ones as expected for geometrical dispersion; it is also slightly larger for the 1000 ppm polymer solution than for the 500 ppm one. At high Péclet numbers and as expected for Taylor dispersion, l_d decreases significantly as the polymer concentration increases from 0 to 1000 ppm. As a result, the experimental curves corresponding to the different solutions cross each other for $Pe \simeq 70$.

[33] In previous experiments with flat smooth walls [*Boschan et al.*, 2003], only Taylor dispersion was observed with a magnitude in agreement with theoretical expectations both for Newtonian and shear thinning fluids.

5.3. Geometrical Dispersion Component for Newtonian Fluids

[34] In order to compare the above experimental values of the dimensionless coefficient α_G to the predictions of equation (3) discussed in section 2 [see *Roux et al.*, 1998], both ε and ξ must be estimated. Experimentally, the determination of such quantities would require first a full determination of the 3D velocity field in the fracture aperture: this is not an easy task, particularly near the walls where the velocity gradients are large and optical observations are difficult. Numerical simulations provide an alternative approach to estimate these quantities which provides a theoretical dispersivity value to be compared to the experimental measurements.

[35] The two-dimensional lattice BGK method has been used to compute the velocity field (however, at present, it is only usable in the Newtonian case). The Brinkman equation was solved using this method for a permeability field derived from the aperture map in the experiment. A detailed description of the technique is given by *Talon et al.* [2002]. The Brinkman coefficient is chosen such that the typical Brinkman length is of the order of the mean aperture. A typical map of the magnitude of the longitudinal velocity component is displayed in Figures 6a–6b together with a view of the concentration front in a simulated displacement experiment. Streaks of low and high velocity are observed in Figure 6a with a length equal to a few times the spacing between the obstacles while the concentration distribution (Figure 6b) is very similar to that observed experimentally. After the velocity field has been determined, its auto-correlation function $R_{vv}(\vec{\delta})$ [*Kitanidis*, 1997] is computed for lags $\vec{\delta}$ both parallel and perpendicular to the flow.

[36] The result is displayed in Figure 7 and the longitudinal auto-correlation function is well fitted by a Gaussian variation: this fit corresponds to a relative amplitude $\varepsilon^2 = 0.17$ of the velocity fluctuations and to a longitudinal normalized correlation length $\xi/a = 2.65$. This leads to a theoretical estimation $\alpha_G = 0.45$ very similar to the experimental value obtained for the Newtonian fluid. The parameter α_G could also be estimated directly from the simulations of Figure 6b: the values obtained vary with the measurement time but remain equal to the theoretical one within ±10%.

5.4. Geometrical Dispersion Component Dependence on Rheology

[37] Experimentally, the dimensionless coefficient α_G characterizing the geometrical dispersion component

Table 2. Values of the Parameters α_G and α_T in (Standard Errors $\delta\alpha_G$ and $\delta\alpha_T$) Used to Fit the Experimental Variations of l_d With Pe for Water Glycerol (*WG*), and 500 ppm (500) and 1000 ppm (1000) Polymer Solutions

Fluids	α_G	$\delta\alpha_G$	α_T	$\delta\alpha_T$	α_G/α_T
WG	0.47	0.04	51.10^{-4}	2.10^{-4}	92
500	0.67	0.05	38.10^{-4}	4.10^{-4}	177
1000	0.71	0.03	17.10^{-4}	2.10^{-4}	417

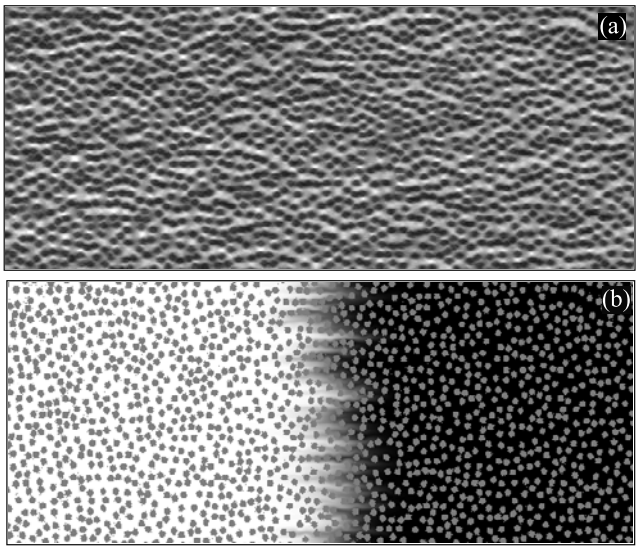

Figure 6. (a) Grey scale map of the longitudinal velocity component (averaged over the local aperture) in a numerical flow simulation using the same geometry as the experiments. Black, zero velocity; white, velocity higher than twice the mean velocity in the model. (b) Dye concentration map of a simulated miscible displacement experiment. Flow is from left to right and medium gray dots indicate the obstacles.

increases with the polymer concentration (see Table 2). In the model of Roux et al. [*Roux et al.*, 1998], α_G is related to the correlation length ξ and to the fluctuations amplitude ε of the velocity by equation (3).

[38] It has been shown [*Boschan et al.*, 2007] that, for shear-thinning fluids with a power law rheological characteristic ($\eta \sim \dot{\gamma}^{n-1}$), the velocity fluctuation $\varepsilon = \sigma_u/u$ should increase by a factor $(1 + n)/2n$ compared to the Newtonian case. From equation (3), assuming that ξ retains the same value for all three solutions, and using the values from Table 1, α_G might therefore be expected to increase by a factor $(n + 1)/n$ from the Newtonian case. The corresponding values for the 500 and 1000 ppm polymer solutions are respectively 3.6 and 4.8. The experimental values of α_G do increase indeed significantly with the polymer concentration but only by smaller respective factors 1.42 and 1.51.

[39] An explanation of this difference may be the fact that the experimental values of α_G are determined by a fit over the full range of *Pe* values investigated. From equation (5), depending on the value of the shear rate $\dot{\gamma}$, the effective viscosity η is constant (Newtonian regime for $\dot{\gamma} \ll \dot{\gamma}_o$) or decrease with $\dot{\gamma}$ following a power law ($\dot{\gamma} \gg \dot{\gamma}_o$). In section 3.2, the transition Péclet number *Pe** between these two regimes has been estimated for the faster channels between the obstacles; the corresponding values are $Pe^* \simeq 10$ and $Pe^* \simeq 30$ respectively for the 1000 ppm and 500 ppm solution. For a variation of *Pe* from $Pe \ll Pe^*$ to $Pe \gg Pe^*$, α_G should increase from the same value as for a Newtonian fluid toward the higher one discussed above [*Auradou et al.*, 2008]. Since the above estimations of *Pe** are within the experimental range, the coefficients α_G obtained from a fit of the variation of l_d/a over data points corresponding to all Péclet numbers will therefore be intermediate between the values for Newtonian and power law fluids as is indeed observed.

[40] Other factors may influence the value of α_G: first, in slower flow regions above the obstacles, the transition toward the power law rheological regime takes place at higher *Pe* values (based on the mean flow velocity) than in the faster channels between the obstacles. Also, in rough model fractures *Boschan et al.* [2007], the influence of small scale velocity gradients has been shown to be reduced by momentum transfer transverse to the main flow for the more concentrated polymer solution. This may also contribute to reduce the value of α_G.

5.5. Taylor Dispersion Component

[41] As noted above, the variations of the dispersivities l_d with the Péclet number measured for the three fluids cross each other (see Figure 5); also, the value of l_d for the Newtonian solution is larger than those corresponding to the polymer fluids at high *Pe* values. Still, for all three fluids, the dispersivity variations are well adjusted by a linear function showing that, in this range of *Pe* values, mixing is largely controlled by Taylor dispersion.

[42] The corresponding dimensionless coefficient α_T depends significantly on the fluid rheology (see Table 2). For a Newtonian fluid flowing between two parallel flat plates [*Aris*, 1956], α_T is equal $1/210 \simeq 0.0047$; this value is close to that measured here for the Newtonian solution (see Table 2).

[43] For shear-thinning fluids, the flattening of the velocity profile in the center of the fracture gap reduces Taylor dispersion so that $\alpha_T < 1/210$. More precisely, in a parallel plate geometry, the dispersion coefficient is related to the velocity profile by the relation [*Bird et al.*, 1987]:

$$D = \frac{2}{aD_m} \int_0^{a/2} dy \left[\int_0^y (v_x(\xi) - U)\, d\xi \right]^2 \tag{7}$$

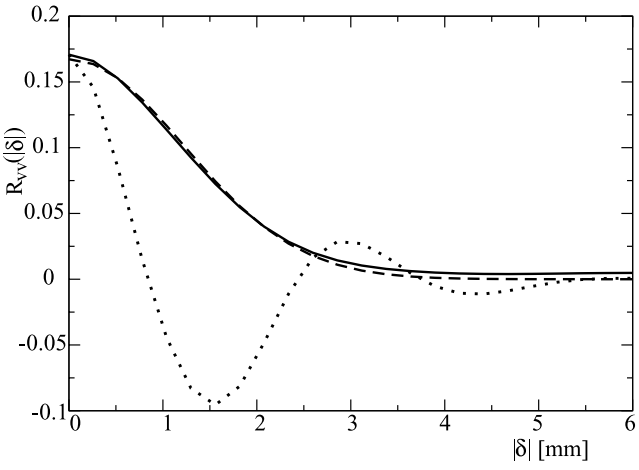

Figure 7. Autocorrelation function of the velocity component parallel to the mean flow as a function of the amplitude $|\delta|$ of the lag for numerical simulations of the type displayed in Figure 6. Solid line, lag $\vec{\delta}$ parallel to the mean flow (dotted line, $\vec{\delta}$ transverse to the flow). Dashed line, Gaussian fit by function: $R = \varepsilon^2 \exp(-|\vec{\delta}|^2/\xi^2)$ with $\varepsilon^2 = 0.17$ and $\xi = 2.65\, a$.

For power law fluids such that $\eta \propto \dot{\gamma}^{n-1}$, $v_x(y)$ can be computed analytically and α_T is found to satisfy the following analytical relation [*Boschan et al.*, 2003]

$$\alpha_T = \frac{n^2}{6(2+5n)(1+4n)}. \quad (8)$$

Using the exponents n listed in Table 1, leads to theoretical predictions $\alpha_T = 17 \times 10^{-4}$ and $\alpha_T = 24 \times 10^{-4}$ respectively for the 1000 and 500 ppm polymer solutions: the first value is similar to the corresponding experimental one and the second is slightly lower (see Table 2). This latter difference may reflect a transition between the "Newtonian plateau" and "power law" regimes due to the larger value of $\dot{\gamma}_0$ for the 500 ppm solution.

6. Front Contours

[44] In the previous section, we have studied local dispersion from the concentration variation profiles along lines of pixels parallel to the mean flow. These display a diffusive spreading resulting from the combination of Taylor and geometrical dispersion. These *local* dispersion processes leave however aside variations of the concentration distribution in the direction perpendicular to the mean flow. The latter inhomogeneities are reflected, for instance, by the filamentary structures displayed in Figure 2 and are due to velocity contrasts between adjacent streamlines. These effects are analyzed here from the dependence of the geometry of the front contours on the time t and on the fluid rheology: the contour is defined as the set of points of coordinates $(x_f(y, t), y)$ for which the mean transit time obtained from the fits of Figure 3 is equal to t (see Figure 8). The contour $x_f(y, t)$ closely coincides here with the normalized isoconcentration lines $c(x_f, y, t) = 0.5$ (white dots in Figure 8). Figure 9 compares contour geometries observed for two different solutions and Péclet numbers at a distance from the inlet close to half the total length. Qualitatively, the global width of the front parallel to the flow increases strongly with the Péclet number Pe and, also, is significantly larger for the shear-thinning solution than for the Newtonian one, particularly at the higher Pe's. This latter increase is due mainly to the growth of the largest structures of the front: smaller features are, on the contrary, less visible (particularly at high Pe) for the shear thinning solution than for the Newtonian one. A qualitatively similar behavior has been reported for channelized self-affine fractures by *Boschan et al.* [2007]. Finally, the locations of the geometrical features of the front contour at high and low Péclet numbers are very strongly correlated for the shear thinning solution; for the Newtonian solution, they often occur at different distances across the front and the correlation between these distances at different Péclet numbers is less visible.

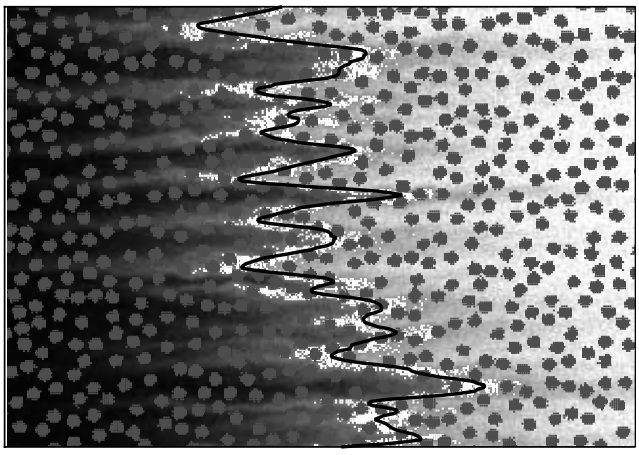

Figure 8. Experimental relative concentration field for a mean front displacement of half the fracture length (500 ppm polymer solutions at $Pe = 345$). Mean flow is horizontal and from left to right. Gray levels, values of the normalized dye concentration $c(x, y, t)$ (white, $c = 0$; black, $c = 1$). Size of field of view: 54.5 mm × 75 mm. Solid line, front contour $x_f(y, t)$ determined from mean transit time; white dots, pixels for which $c(x, y, t) = 0.50 \pm 0.03$. Large dark gray dots, cylindrical obstacles (these are not perfectly circular due to the limited resolution of the image).

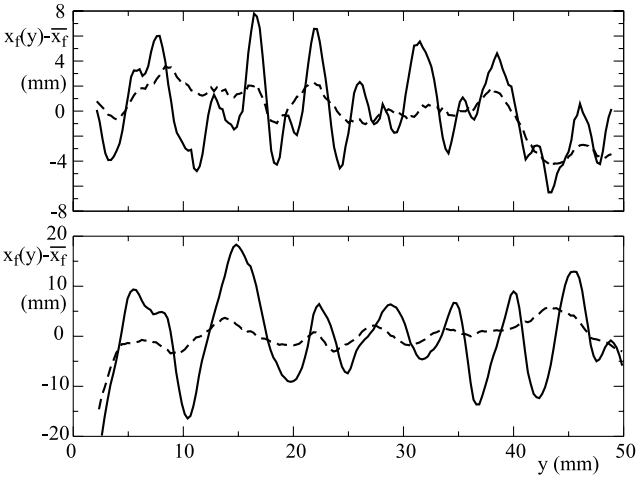

Figure 9. Front geometries for a mean distance from the inlet equal to half the fracture length. Top graph: Newtonian water-glycerol solution. Solid line, $Pe = 450$; dashed line, $Pe = 8.6$. Bottom graph, 1000 ppm polymer solution. Solid line, $Pe = 345$; dashed line, $Pe = 6.6$.

[45] Quantitatively, the width of the front is characterized in the following by the standard deviation $\sigma(t) = \langle (x_f(y, t) - \overline{x_f}(t))^2 \rangle_y^{0.5}$ of the coordinates $x_f(y, t)$ of the points of the front; $\overline{x_f}(t)$ is the average with respect to y of $x_f(y, t)$. The variation of $\sigma(t)$ with $\overline{x_f}(t)$ is displayed in Figure 10. At short distances, σ increases with $\overline{x_f}$ for the two polymer solutions while it reaches almost immediately a lower limiting value $\sigma_\infty = 2.5$ mm for the Newtonian one. Moreover, the value of σ_∞ is higher (7.5 mm) and reached after a longer distance for the 1000 ppm concentration than for the 500 ppm one (5 mm). All data points correspond to the same flow velocity but the Péclet number is higher for the water-glycerol than for the water-polymer solutions due to its higher viscosity (and therefore lower molecular diffusion coefficient).

[46] The standard deviation σ also reaches a limit σ_∞ at long enough distances for all Pe values and for the three fluids investigated (see inset of Figure 10 for the 500 ppm solution). Finally, σ_∞ increases significantly with the Péclet

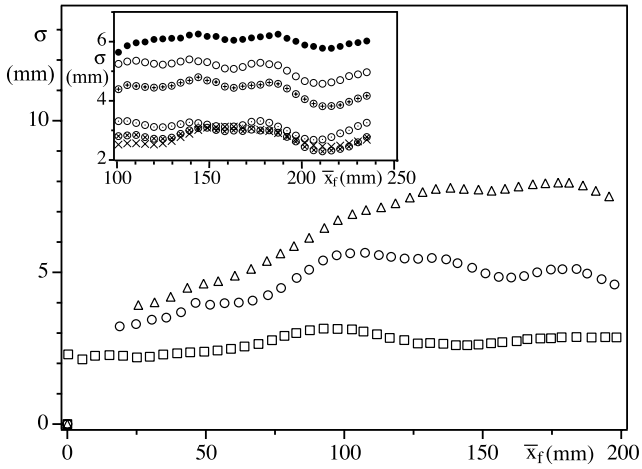

Figure 10. Variation of the front width σ as a function of the mean distance $\overline{x_f}$ from the inlet for the water-glycerol solution (square) (Pe = 90) and the 500 ppm (open circle) and 1000 ppm (open triangle) polymer solutions (Pe = 69). Inset, variation of σ as a function of $\overline{x_f}$ for the 500 ppm polymer solution at Péclet numbers (from top to bottom): Pe = 345 (solid circle), Pe = 172 (open circle), Pe = 69 (plus in open circle), Pe = 34 (dot in open circle), Pe = 17 (cross in open circle), Pe = 6.6 (cross).

number, in agreement with the qualitative observations on Figure 9.

[47] These latter features of the variation of σ with distance differ completely from previous observations on channelized self-affine fractures *Boschan et al.* [2007] in which σ increases linearly with distance over the full length of the model. This implies that transverse exchange is more effective in the present case due to the smaller characteristic distance of the velocity variations in the transverse direction. Also, the analysis of the geometry of the front displayed in Figure 11 suggests that the characteristic transverse size of the fingers is larger for the polymer solutions (∼5 mm) than for the Newtonian ones (∼3 mm). Assuming that this reflects a larger transverse correlation length of the velocity would then explain why a longer path length is required to reach the limit σ_∞.

[48] Figure 11 displays the variation of the standard deviation σ_∞ in the stationary regime as a function of Pe for the three solutions. A logarithmic horizontal scale is used, showing that σ_∞ varies roughly logarithmically with Pe: in these coordinates, the slope of the variation is respectively 3.7 times and 2.5 times higher for the 1000 ppm and 500 ppm polymer solutions than for the water-glycerol one.

7. Discussion and Conclusion

[49] The present work has demonstrated the characteristic features of miscible displacement fronts and of the flow distribution in single fractures with a random distribution of cylindrical obstacles of uniform size. Using a transparent model fracture and optical tracer concentration measurements, we could measure dispersion at both the local and global scales and to analyze in detail the geometry of the displacement front and its variation with time. The dispersion characteristics differ strongly both from the case of homogeneous 3D porous media and from the recent experiments of *Boschan et al.* [2007] on model fractures with self affine walls and a channelized aperture field.

[50] In both types of model fractures, the local dispersivity l_d can be determined from the time variation of the concentration $c(x, y, t)$ on individual pixels which satisfies the convection-diffusion equation (1). In the present case, the variation of l_d with the Péclet number reflects a combination of geometrical and Taylor dispersion in agreement with previous dispersion measurements [*Ippolito et al.*, 1994; *Detwiler et al.*, 2000] on similar systems. Geometrical dispersion is dominant at low Péclet numbers ($Pe \lesssim 20$) for which Taylor dispersion is small and l_d is nearly constant with Pe: this contribution of geometrical dispersion increases with the shear-thinning character of the fluids which amplifies spatial velocity fluctuations. Taylor dispersion is dominant at high Péclet numbers ($Pe \gtrsim 100$) and is significantly reduced for shear-thinning fluids due to the flattening of the velocity profiles (the estimation of this variation agrees with the experimental observations for the 1000 ppm solution). As a consequence of the above features, the variations of l_d with Pe cross each other at intermediate Péclet numbers (Figure 5).

[51] In the channelized self affine fractures studied by *Boschan et al.* [2007], on the contrary, local dispersion corresponds solely to the Taylor mechanism (and molecular diffusion for $Pe \lesssim 1$). This reflects the different values of the correlation length ξ of the flow velocity field in the two types of models. In the present work, both ξ and the relative amplitude of the velocity fluctuations have been determined in the Newtonian case by simulating numerically the flow field using a lattice-Boltzmann method, leading to $\xi/a \simeq 2.5$ (a is the mean aperture). Using equation (3), this provides a theoretical value of the geometrical normalized dispersivity component α_G in good agreement with the experimental dispersivity measurements at low Péclet numbers $Pe \lesssim 20$ for which geometrical dispersion is dominant. In the channelized model used by *Boschan et al.* [2007], the correlation length of the velocity field is much larger (of the order of

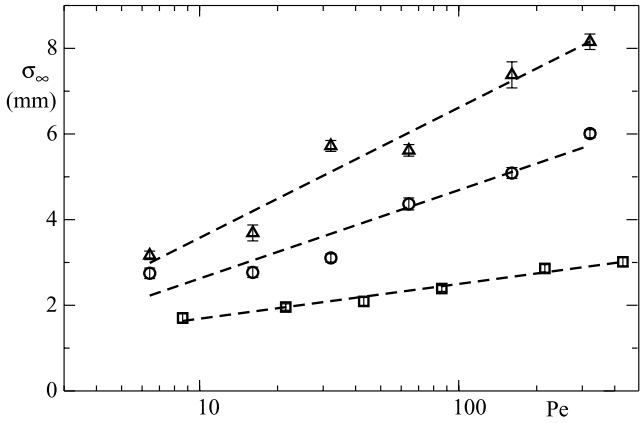

Figure 11. Variation of the front width σ_∞ (averaged other all fronts corresponding to the stationary regime in each experiment) as a function of Pe. The symbols for the different solutions are the same as in Figure 10 (main graph). Dashed lines correspond to fits with the following variations: σ_∞ = 1 + 0.8 Log(Pe) (water-glycerol); σ_∞ = 0.6 + 2 *Log* (Pe) (500 ppm) and σ_∞ = 0.6 + 3 Log (Pe) (1000 ppm polymer solutions).

the length of the sample) and a local mechanical dispersion regime cannot get established.

[52] Comparisons with simple homogeneous 3*D* porous media indicate another difference: in that case, Taylor dispersion is not visible, even at high Péclet numbers and geometrical dispersion is dominant as long as $Pe \gtrsim 1$ [*Bear*, 1972]. This results from the multiply connected topology of usual 3*D* porous media: it prevents Taylor dispersion due to the flow profile in individual channels to appear since tracer particles only remain generally close to a wall or in the center of a flow channel for a short distance. In intermediate geometries such as 2*D* networks of channels of random aperture [*Bruderer and Bernabé*, 2001; *D'Angelo et al.*, 2007] which may be considered as a model of fractures with a distribution of contact points, a variation of l_d with the Péclet number as $Pe^{0.35}$ has been observed at medium and high flow rates. This is intermediate between the exponents corresponding to geometrical and Taylor dispersion and results from the 2*D* nature of the network.

[53] At the global scale the front displays only small elongated narrow structures. This contrasts with the self-affine channelized fractures studied by *Boschan et al.* [2007] for which large scale features of the front with a width parallel to the flow increasing linearly with the distance from the inlet are visible. In the present study the width σ of the front structures parallel to the flow reaches at long distances a limit σ_∞ varying logarithmically with *Pe* and increasing for shear thinning fluids; practically, σ is determined from the geometry of lines of equal mean transit time $\bar{t}(x, y)$. Here, σ ranges from 1 to 2 times the mean spacing of the obstacles; further experiments with different sizes and distributions would be needed to determine the relation, if any, between σ and the geometrical parameters of the model fracture. These results imply that transverse mixing is effective enough to allow for tracer exchange between adjacent streamlines of different velocities and limit the growth of the fingers. The slow increase of σ_∞ with *Pe* suggests that mixing is less effective at high velocities (perhaps because it involves transverse molecular diffusion). On the contrary for channelized self-affine fractures, characteristic distances are larger and do not allow for transverse mixing: in this case spreading is convective and σ increases linearly with distance.

[54] Regarding the influence of the rheology, both σ_∞ and the distance needed to reach this limit are larger for shear thinning solutions: this reflects likely an enhancement of the velocity contrasts between the different front structures. For similar reasons, for channelized self-affine fractures, the global front width is also larger for shear thinning solutions.

[55] Overall, the results of this study and their comparison with experiments realized with self-affine fracture models demonstrate the key influence of the geometry of the wall roughness and of the distribution of its characteristic length scales. In this respect, they provide guidelines for future work on more natural systems as well as numerical simulations. While Taylor dispersion is always present, flow velocity variations may lead either to global convective front deformations for channelized flows as in self-affine fractures or to diffusive geometrical spreading as here. Understanding these mechanisms was made possible by diagnostic techniques analyzing the concentration distributions in a broad range of lengths scales. Comparing shear-thinning and Newtonian fluids may also represent a very useful diagnostic tool to investigate transport in fractured media since they influence in opposite ways geometrical and Taylor dispersion.

[56] **Acknowledgments.** The work of HA and JPH is funded by the EHDRA (European Hot Dry Rock Association) in the framework of the STREP Pilot plan program SES6-CT-2003-502706) and by the CNRS-PNRH program. This work was also supported by a CNRS-Conicet Collaborative Research Grant (PICS no. 2178) and by the ECOS Sud program no. A03E02 and the UBA grant I029.

References

Adler, P. M., and J.-F. Thovert(1999), *Fractures and Fracture Networks*, Springer, Dordrecht, Netherland.

Aris, R. (1956), On the dispersion of a solute particle in a fluid moving through a tube, *Proc. R. Soc., Ser. A*, *235*, 67–77.

Auradou, H., G. Drazer, J. P. Hulin, and J. Koplik (2005), Permeability anisotropy induced by a shear displacement of rough fractured walls, *Water Resour. Res.*, *41*, W09423, doi:10.1029/2005WR003938.

Auradou, H., G. Drazer, A. Boschan, J. P. Hulin, and J. Koplik (2006), Flow channeling in a single fracture induced by shear displacement, *Geothermics*, doi:10.1016/j.geothermics.2006.11.004.

Auradou, H., A. Boschan, R. Chertcoff, S. Gabbanelli, J. P. Hulin, and I. Ippolito (2008), Velocity contrasts enhancement for shear thinning solutions flowing in a rough fracture, *J. Non Newtonian Fluid Mech.*, doi:10.1016/j.jnnfm.2007.11.008.

Bear, J. (1972), *Dynamics of Fluids in Porous Media*, 764 pp., Elsevier, New York.

Berkowitz, B. (2002), Characterizing flow and transport in fractured geological media: A review, *Adv. Water Resour.*, *25*, 861–884.

Bird, R. B., R. C. Armstrong, and O. Hassager (1987), *Dynamics of Polymeric Liquids*, 2nd ed., vol. 1, Chap. 4, 649 pp., John Wiley, Hoboken, N. J.

Borden, R. C. (2007), Effective distribution of emulsified edible oil for enhanced anaerobic bioremediation, *J. Contam. Hydrol.*, *94*, 1–12.

Boschan, A., V. J. Charette, S. Gabbanelli, I. Ippolito, and R. Chertcoff (2003), Tracer dispersion of non-Newtonian fluids in a Hele-Shaw cell, *Physica A*, *327*, 49–53.

Boschan, A., H. Auradou, I. Ippolito, R. Chertcoff, and J. Hulin (2007), Miscible displacement fronts of shear-thinning fluids inside rough fractures, *Water Resour. Res.*, *43*, W03438, doi:10.1029/2006WR005324.

Bouchaud, E. (2003), The morphology of fracture surfaces: A tool for understanding crack propagation in complex materials, *Surf. Rev. Lett.*, *10*, 797–814.

Bragato, M., and O. A. El Seoud (2003), Formation, properties and "ex situ" soil decontamination by vegetable oil-based microemulsions, *J. Surf. Det.*, *6*, 143–150.

Brown, S., A. Caprihan, and R. Hardy (1998), Experimental observation of fluid flow channels in a single fracture, *J. Geophys. Res.*, *103*, 5125–5132.

Bruderer, C., and Y. Bernabé (2001), Network modeling of dispersion: Transition from Taylor dispersion in homogeneous networks to mechanical dispersion in very heterogeneous ones, *Water Resour. Res.*, *37*, 897–908.

D'Angelo, V., H. Auradou, C. Allain, and J.-P. Hulin (2007), Pore scale mixing and macroscopic solute dispersion regimes in polymer flows inside two-dimensional model networks, *Phys. Fluids*, *19*, 033103, 1–10.

Detwiler, R. L., L. Russel, S. E. Pringle, E. Scott, and R. J. Glass (1999), Measurement of fracture aperture fields using transmitted light: An evaluation of measurement errors and their influence on simulations of flow and transport through a single fracture, *Water Resour. Res.*, *35*, 2605–2617.

Detwiler, R., H. Rajaram, and R. J. Glass (2000), Solute transport in variable aperture fractures: An investigation of the relative importance of Taylor dispersion and macrodispersion, *Water Resour. Res.*, *36*, 1611–1625.

Drazer, G., and J. Koplik (2002), Transport in rough self-affine fractures, *Phys. Rev. E*, *66*, 026303.

Gabbanelli, S., G. Drazer, and J. Koplik (2005), Lattice Boltzmann method for non-Newtonian (power-law) fluids, *Phys. Rev. E*, *72*(4 Part 2), Oct.

Gelhar, L. W. (1993), *Stochastic Subsurface Hydrology*, Prentice-Hall, Upper Saddle River, N. J.

Gentier, S., E. Lamontagne, G. Archambault, and J. Riss (1997), Anisotropy of flow in a fracture undergoing shear and its relationship to the

direction of shearing and injection pressure, *Int. J. Rock Mech. Min. Sci.*, *34*(3–4), 412.

Horobin, R. W., and J. A. Kiernan (Eds.) (2002), *Conn's Biological Stains: A Handbook of Dyes, Stains and Fluorochromes for Use in Biology and Medicine*, BIOS Scientific, London.

Ippolito, I., E. J. Hinch, G. Daccord, and J. P. Hulin (1993), Tracer dispersion in 2-D fractures with flat and rough walls in a radial flow geometry, *Phys. Fluids A*, *5*(8), 1952–1961.

Ippolito, I., G. Daccord, E. J. Hinch, and J. P. Hulin (1994), Echo tracer dispersion in model fractures with a rectangular geometry, *J. Contam. Hydrol.*, *16*(8), 1952–1961.

Kitanidis, P. K. (1997), *Introduction to Geostatistics*, Cambridge Univ. Press, New York.

NAS Committee on Fracture Characterization and Fluid Flow (1996), *Rock Fractures and Fluid Flow: Contemporary Understanding and Applications*, National Academy Press, Washington, D. C.

Neretnieks, I. (2002), A stochastic multi-channel model for solute transport-analysis of tracer tests in fractured rock, *J. Contam. Hydrol.*, *55*, 175–211.

Paterson, A., A. D'Onofrio, C. Allain, and J. P. Hulin (1996), Tracer dispersion in a polymer solution flowing through a double porosity porous medium, *J. Phys. II*, *6*, 1639–1654.

Roux, S., F. Plouraboué, and J. P. Hulin (1998), Tracer dispersion in rough open cracks, *Transp. Porous Media*, *32*, 97–116.

Talon, L., J. Martin, N. Rakotomalala, D. Salin, and Y. C. Yortsos (2002), Lattice BGK simulations of macrodispersion in heterogeneous porous media, *Water Resour. Res.*, *39*(5), 1135, doi:10.1029/2002WR001392.

Taylor, G. I. (1953), Dispersion of soluble matter in solvent flowing slowly through a tube, *Proc. R. Soc., Ser. A*, *219*, 186–203.

Tsang, Y. W., and C. F. Tsang (1987), Channel model of flow through fractured media, *Water Resour. Res.*, *23*(3), 467–479.

Vartuli, M., J.-P. Hulin, and G. Daccord (1995), Taylor dispersion in a polymer solution flowing in a capillary tube, *AIChE J.*, *41*(7), 1622–1628.

Witherspoon, P. A., C. F. Tsang, C. F. Tsang, and J. E. Gale (1980), Validity of cubic law for fluid flow in a deformable rock fracture, *Water Resour. Res.*, *16*, 1016–1024.

Yeo, I. W., M. H. De Freitas, and R. W. Zimmerman (1998), Effect of shear displacement on the aperture and permeability of a rock fracture, *Int. J. Rock Mech. Min. Sci.*, *35*(8), 1051–1070.

H. Auradou, J. P. Hulin, and L. Talon, Laboratoire FAST, Bâtiment 502, Campus Paris Sud, 91405 Orsay Cedex, France. (auradou@fast.u-psud.fr)

A. Boschan, R. Chertcoff, and I. Ippolito, Grupo de Medios Porosos, Facultad de Ingeniería, Universidad de Buenos Aires, Paseo Colón 850, 1063 Buenos Aires, Argentina.